ACS APPLIED MATERIALS & INTERFACES

www.acsami.org

Research Article

Strain-Modulated Interlayer Charge and Energy Transfers in MoS_2/WS_2 Heterobilayer

Joon-Seok Kim,* Nikhilesh Maity, Myungsoo Kim, Suyu Fu, Rinkle Juneja, Abhishek Singh,* Deji Akinwande,* and Jung-Fu Lin*

Cite This: *ACS Appl. Mater. Interfaces* 2022, 14, 46841−46849

Read Online

ACCESS | Metrics & More | Article Recommendations | Supporting Information

ABSTRACT: Excitonic properties in 2D heterobilayers are closely governed by charge transfer (CT) and excitonic energy transfer (ET) at van der Waals interfaces. Various means have been employed to modulate the interlayer CT and ET, including electrical gating and modifying interlayer spacing, but with limited extent in their controllability. Here, we report a novel method to modulate these transfers in the MoS_2/WS_2 heterobilayer by applying compressive strain under hydrostatic pressure. Raman and photoluminescence measurements, combined with density functional theory calculations, show pressure-enhanced interlayer interaction of the heterobilayer. Heterobilayer-to-monolayer photoluminescence intensity ratio (η) of WS_2 decreases by five times up to ≈4 GPa, suggesting enhanced ET, whereas it increases by an order of magnitude at higher pressures and reaches almost unity. Theoretical calculations show that orbital switching and charge transfers in the heterobilayer's hybridized conduction band are responsible for the non-monotonic modulation of the transfers. Our findings provide a compelling approach toward effective mechanical control of CT and ET in 2D excitonic devices.

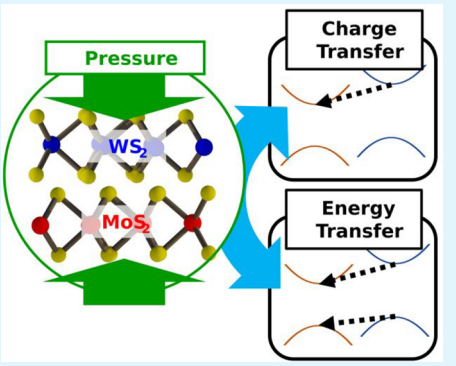

KEYWORDS: *Heterobilayer, Strain Engineering, Diamond Anvil Cell, Density Functional Theory, Charge Transfer, Energy Transfer*

INTRODUCTION

The ability to couple and control exciton emission is a keystone challenge for realizing excitonic solid state devices, where the computational and transmittance efficiencies are anticipated to be greatly enhanced.[1,2] In light of the exciton control, two-dimensional (2D) materials are attracting significant interest as an optimal material system, owing to their strong light−matter interaction and large excitonic binding energies.[3,4] Combined with the ability to selectively stack a wide variety of atomic layers, 2D heterostructures possess great potential to be employed in excitonic device applications.[5−8] For example, electrical transport control of the interlayer excitons, where bound electrons and holes reside in the opposite layers, has been achieved in type-II transition metal dichalcogenide (TMDC) heterostructures.[6,7] The successful control of the interlayer excitons further implies the possibility of controlling the excitonic behavior by modulating interlayer charge transfer (CT) and excitonic energy transfer (ET). In this study, we present modulation of the interlayer CT and ET by applying compressive strain to tune the van der Waals (vdW) interaction between WS_2 and MoS_2 monolayers under hydrostatic pressures. Our combined experimental and theoretical results show that the interlayer interaction is enhanced as the normal compressive strain is applied, leading to an effective modulation of the CT and ET. As a result, the photoluminescence (PL) enhancement factor was tuned by more than an order of magnitude.

Charge transfers in 2D heterobilayers, where electrons (holes) in one of the monolayers with a higher conduction band minima CBM (lower valence band maxima VBM) are transferred to the other monolayer, occur on the time scale of subpicoseconds, regardless of the momentum mismatch between the layers.[9,10] Energy transfers in 2D heterobilayers, on the other hand, occur without net charge transfer between the layers, either by transfer of a set of electrons and holes (Dexter-type) or by a dipole coupling (Förster-type).[11,12] The dominant ET mechanism in a 2D heterobilayer may depend on the type of band alignment and is a subject of ongoing research: In type-I heterostructures, photoexcited free electrons and holes reportedly transfer from the high-band gap to low-band gap layer, i.e., Dexter-type being dominant mechanism.[13] In type-II heterostructures where CBM and VBM lie on the opposite layer, Förster-type energy transfer is suggested to be dominant, but thermally assisted charge transfer can still contribute depending on the band alignments.[11,14]

Received: June 20, 2022
Accepted: September 26, 2022
Published: October 4, 2022

https://doi.org/10.1021/acsami.2c10982
ACS Appl. Mater. Interfaces 2022, 14, 46841−46849

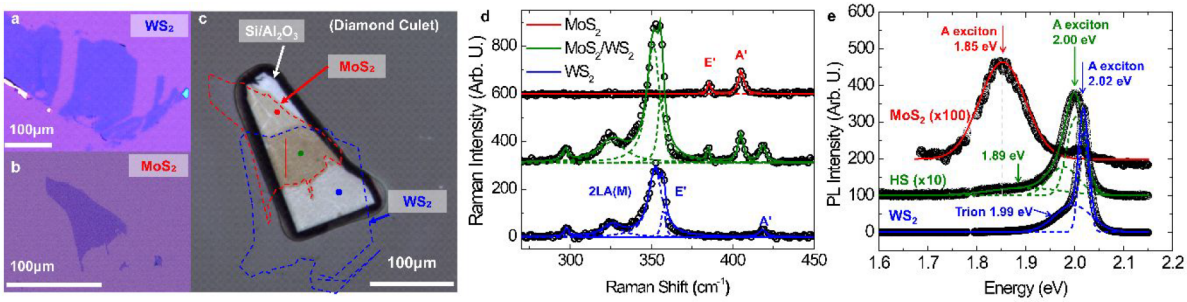

Figure 1. Preparation and ambient-pressure characterization of the MoS_2/WS_2 heterostructure sample. Monolayer (a) WS_2, (b) MoS_2, and (c) their heterostructure (HS) transferred onto an alumina-coated silicon chip placed on a diamond culet. Red and blue dashed lines outline the MoS_2 and WS_2 monolayer, respectively, while their overlapping area represents the heterostructure. The red, blue, and green dots indicate the spots where Raman and PL spectra were taken for MoS_2-only, WS_2-only, and HS regions, respectively, throughout the entirety of the experiments. (d) Raman spectra of the monolayers and the HS, showing characteristic in-plane E′, out-of-plane A′, and second-order longitudinal acoustic LA(M) peaks. (e) photoluminescence (PL) spectra of the monolayers and HS.

Regardless of the dominant mechanism, CT and ET between two 2D materials are strongly governed by the interaction at the vdW interface. Various approaches have been taken to engineer the vdW interaction in the 2D materials system, such as thermal annealing,[15] surface termination,[16] intercalations,[17] interlayer spacing,[11,12] and electrical gating.[18,19] Intriguingly, mechanical strain provides an effective and chemically inert modulation of the interlayer interaction.[20,21] For instance, Pak et al. (2017) reported, by comparing the strain-dependence of Raman shift and optical band gap energies, that the interlayer coupling in an epitaxially grown MoS_2/WS_2 sample enhances under uniaxial tensile strain due to the reduced interlayer S−S bond lengths.[22] Another clear indication of the interaction modulation can be found in the reports for the band gap evolution of semiconducting TMDCs under hydrostatic pressure: Multilayer semiconductor TMDCs turn metallic as applied pressure enhances the interlayer electronic interactions between sulfur and molybdenum atoms,[23] whereas the band gaps in monolayers open up with increasing pressure before it starts to close down at much higher pressures.[24,25] Hydrostatic pressure gives access to directly modulating the interlayer van der Waals bond length, which is more compressible than the intralayer covalent bonds and therefore can be more effective in modulating 2D materials' electronic,[26−28] thermal,[29,30] and topological[31,32] properties. Enhancement of the interlayer CTs has also been demonstrated in 2D heterostructure systems, clearly demonstrating the effect of the mechanical strain on the interlayer interaction.[33−35]

Here, we report an effective tuning of the CT and excitonic ET in a MoS_2/WS_2 TMDC heterostructure under hydrostatic pressure. Vibrational properties, band gaps, and interlayer charge/energy transfers in the 1L-MoS_2/1L-WS_2 heterostructure were characterized by Raman and photoluminescence (PL) spectroscopy, combined with diamond anvil cell (DAC) apparatus. At pressures below 4 GPa, the PL intensity of WS_2 in the heterobilayer is strongly quenched compared to that of the stand-alone 1L-WS_2, suggesting the dominant ET in the heterointerface. Interestingly, at pressures above 4 GPa, the heterostructure-to-monolayer PL intensity ratio of WS_2 increases by more than an order of magnitude, whereas the ratio of MoS_2 continues to decrease. Density functional theory (DFT) calculations reveal an enhanced vdW interaction that hybridizes the heterobilayer's energy bands resulting in charge density evolution in the band extrema. The pressure effects are decomposed computationally to distinguish the effective strain component in the heterobilayer. The presented engineering of the vdW interaction and charge/energy transfers suggests a novel mechanism to potentially engineer mechanically controlled optoelectronic devices.[36,37]

RESULTS

Sample Preparation and Initial Characterization. High-quality single-crystal MoS_2 and WS_2 monolayers with lateral dimensions of approximately 100−400 μm were mechanically exfoliated using gold-assisted methods (Figure 1a,b).[38] The MoS_2 and WS_2 monolayers were stacked into a heterostructure (HS) on a Si/Al_2O_3 substrate via the dry-transfer method.[39] The HS on the substrate has long edges of the monolayers aligned to form a twist angle ≈3−5° with an overlapping area of ≈50 μm × 70 μm (Figure 1c). The large lateral dimensions of the heterostructure assured optical observations to be free of effects from possible edge states, grain boundaries, exciton diffusion, and flake-to-flake variations.[40,41] High-purity Ne inert gas was used as the pressure transmitting medium (PTM) in order to exert quasi-hydrostatic pressure,[42] and to ensure chemical purity in the sample chamber without potential chemical reaction with or contamination of the sample. Note that Si[43] and Al_2O_3[44] do not undergo first-order phase transitions in the pressure range of the present study, leaving indirect bandgap[45] and large bandgap, respectively. The potential heat from the incident laser will effectively dissipate through the bottom diamond anvil or Ne pressure medium, indicating that there is negligible temperature effect on the designed experiment. It is also worth emphasizing that, even though high-vacuum annealing could not be done after the DAC/substrate/sample assembly, the sample's vdW bond lengths are expected to reach reasonably close to the ideal values after initial ∼0.1 GPa compression. This is based on the facts that (i) the monolayers were annealed at high vacuum and high temperature prior to the transfer and therefore were free of residue; (ii) the sequential transfer (details in the Methods section) did not involve any liquid-phase species that may have contaminated the interfaces; and (iii) the pressure employed in our study exceeds by 1−2 orders of magnitude the reported pressure to reduce interlayer spacing to near-ideal values.[20] Consequently, changes in dielectric screening resulting from the 2D-substrate distance change is expected to have limited effect.

https://doi.org/10.1021/acsami.2c10982
ACS Appl. Mater. Interfaces 2022, 14, 46841−46849

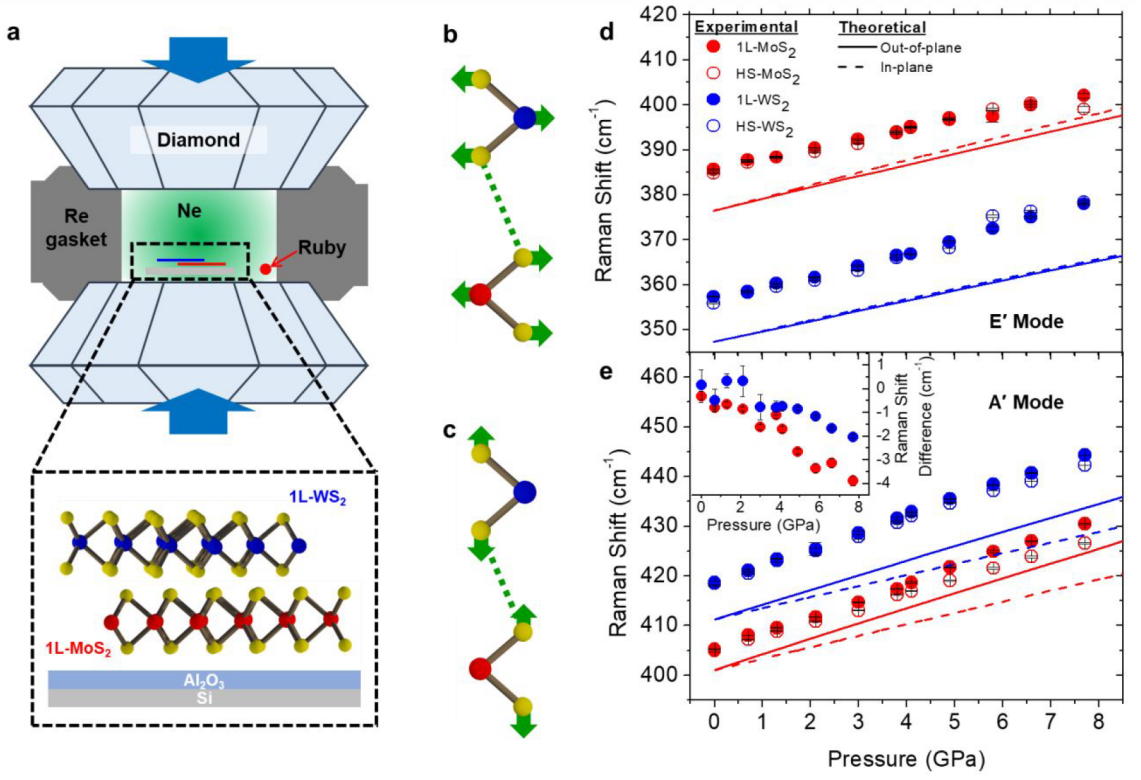

Figure 2. Raman measurements of the 1L-MoS_2/1L-WS_2 heterostructure under hydrostatic pressure. (a) Schematic side view of the sample chamber in a diamond anvil cell (top) and the HS sample on Al_2O_3/Si substrate (bottom). (b) In-plane E′ and (c) out-of-plane A′ Raman modes with dashed lines illustrating the interlayer interaction. (d) In-plane E′ and (e) out-of-plane A′ Raman peak positions from MoS_2 and WS_2, experimentally measured (symbols) and theoretically calculated (lines). Inset of (e) shows the peak position difference of the A′ Raman mode ($\omega_{HS} - \omega_{1L}$). The error bars are standard errors from Lorentzian fits.

Optical characterizations confirmed the uniform monolayer thickness and high quality of the exfoliated flakes in atmospheric pressure, as shown in the sharp Raman spectra (Figure 1d) and uniform Raman intensity maps of A′ peak in 1L-MoS_2 and 1L-WS_2 (Figure S1). The Raman spectra of the heterostructure were a superimposition of individual MoS_2 and WS_2 spectra, with A′, E′, and 2LA(M) peaks present. Monolayer MoS_2 and WS_2 exhibit strong PL signals at the A exciton energies of 1.85 and 2.02 eV, respectively, in highly symmetric Gaussian lineshapes, confirming the high quality nature of the monolayers (Figure 1e). Note that the Au-exfoliated monolayers reportedly have optical quality comparable to the traditional tape-exfoliated counterparts.[46−48] The PL spectrum of the heterostructure shows superimposed spectral signatures of both MoS_2 and WS_2. We note that conclusive signs of interlayer exciton above the noise floor were not observed in our experiments. The absence may be attributed to the combination of the monolayers' off-parallel stacking angle that reportedly reduce the intensity,[49] and ≈2.4-mm-thick diamond anvil elevating the fluorescence noise floor. In addition, interlayer exciton reportedly vanishes at a much lower pressure than intralayer excitons, where the exact reason requires further investigation.[35]

Strain-Modulation of Phonon Dynamics and Band Structures. With hydrostatic pressure applied to the sample using a DAC (Figure 2a), the in-plane E′ and out-of-plane A′ Raman mode (Figure 2b,c) frequencies of the 1L-MoS_2, 1L-WS_2, and their HS blueshift, indicate the compression-induced bond length shortening (symbols in Figure 2d,e and Figure S2). The A′ peaks display significantly higher pressure dependence (≈3.3 cm^{-1} GPa^{-1}) than the E′ peaks (≈2.3 cm^{-1} GPa^{-1}), showing that the hydrostatic pressure is effective in shortening the intralayer S−S distance and modulating the out-of-plane modes. The effective compression of intralayer S−S distance also indicates even higher compression of weaker interlayer vdW force. It is worth noting that the Raman peak shifts under hydrostatic pressure cannot be directly compared to those under in-plane strain. The pressure-dependent strain in the in-plane (*a*-axis) and out-of-plane (*c*-axis) directions may be estimated based on the equation of states of bulk crystals.[23,26] The E′ peaks in the HS show insignificant deviation from those in the monolayers, confirming minimal slippage at the heterointerface. On the other hand, the A′ peaks in the heterostructures are consistently lower than those in the monolayers (inset of Figure 2e), which is an indication of the enhanced interlayer interaction.[23,33] The weaker blueshifts for both MoS_2 and WS_2 A′ modes in the HS contradict with Fu et al.'s report on $MoSe_2$/WSe_2 heterostructure,[35] where the WSe_2 A′ mode in HS further stiffens with pressure. The different behavior may arise from the difference in the A′ mode frequencies of the investigated materials, as Fu et al. argues that the coherent vibration in the bilayer renormalizes and induces the divergence of the A′ modes in HS. In our MoS_2/WS_2 case, the two A′ mode frequencies are apart by a larger frequency (≈15 cm^{-1}) and are less likely to cause coherence. It is also possible that the contradicting pressure-dependencies may arise from differences in experimental setup. For instance, the 2D material's in-plane (*a*-axis) incompressibility matches much better with that of the silicon substrate compared to that of diamond

https://doi.org/10.1021/acsami.2c10982
ACS Appl. Mater. Interfaces 2022, 14, 46841−46849

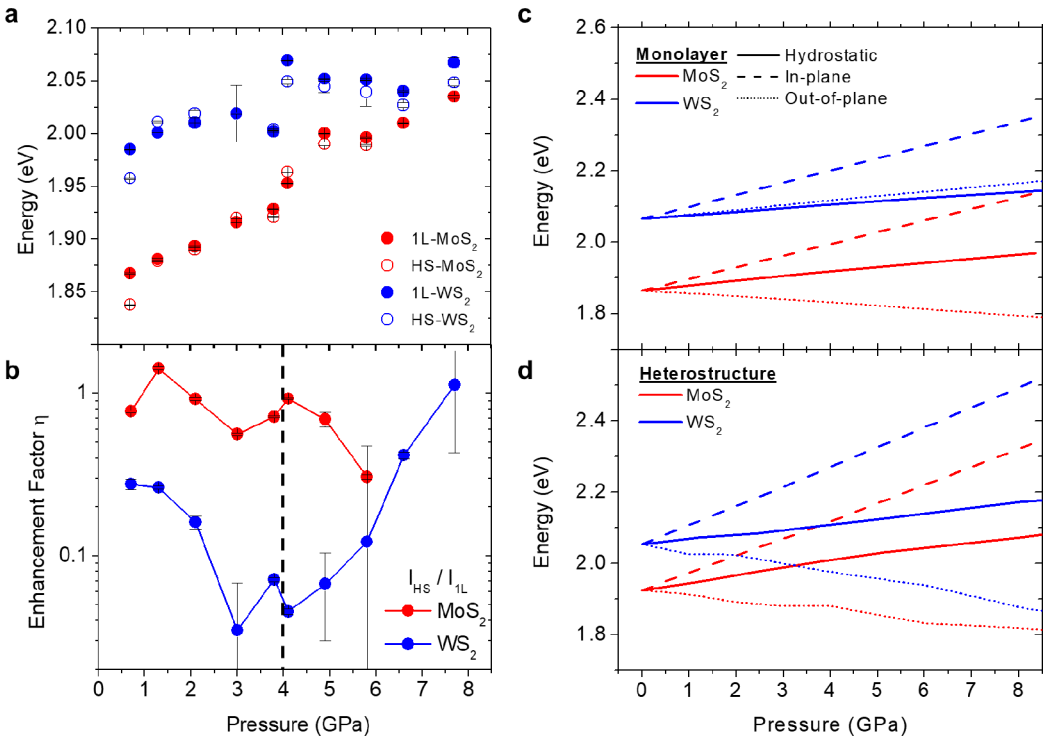

Figure 3. Pressure-dependent evolution of optical band gaps and PL intensity ratio. (a) Optical band gaps of the monolayers and heterostructure measured from the PL spectral peaks as a function of hydrostatic pressure. (b) PL enhancement factor η (I_{HS}/I_{1L}) as a function of pressure. (c,d) Calculated evolution of the A exciton states of (c) individual monolayers and (d) as the heterostructure as a function of pressure (solid lines), and equivalent in-plane (dashed lines) and out-of-plane strains (dotted lines). The error bars in panels a and b are standard errors from Lorentzian fits.

substrate,[26,43,50] and therefore the 2D materials are expected to experience much less shear strain. In addition, Ne pressure medium exhibits lower nonhydrostaticity than Ar,[42] which may have resulted in less inhomogeneity or shear strain.

To computationally model the effect of hydrostatic pressure on the vibrational mode evolution, Raman modes were calculated for the monolayers and the HS (Figure S3), under in-plane strain, out-of-plane strain (lines in Figure 2d,e), and hydrostatic pressure conditions (Figures S5−6 and Table S1). All Raman active modes of monolayers show significant blueshifts with increasing pressure, in good agreement with the experimental observation. For decomposed strain components, it is found that in-plane (dashed lines) and out-of-plane (solid lines) strain components have a similar contribution to the blueshift of the E′ modes, whereas the out-of-plane strain component contributes the most in the A′ mode blueshift. These experimental and computational findings highlight the role of hydrostatic pressure in reducing the interlayer distance and enhancing the out-of-plane interlayer interactions (Figure S7). Details on the computation of active Raman modes and strain components (Note S1, Figure S4) could be found in the Supporting Information.

The optical band gaps of the monolayers and HS are extracted from the Gaussian fitting of the PL spectra at high pressures (Figures S8−9). The band gaps of the MoS_2 in both monolayer and heterostructure increase with increasing pressure with a nearly linear pressure dependence of ≈25.3 meV GPa^{-1}, in good agreement with previous reports (Figure 3a).[24,25] On the other hand, the band gaps of the WS_2 increase until reaching an extremum at ≈4 GPa and then start to moderately decrease with further increase in pressure. The non-monotonic pressure response of the WS_2 band gap can be attributed to the transition from the K−K direct bandgap to the Λ−K indirect bandgap.[51]

Our theoretical calculations also confirm the decomposition of the strain-induced band gap modulation. The evolution of the excitonic energy levels with different strain components shows that the in-plane strain component is most effective in increasing the band gaps (dashed lines in Figure 3c,d, Figures S11), whereas the out-of-plane strain component (dotted lines) suppresses the band gaps. As a result of these competing effects, the hydrostatic pressure increases the band gap, which is in good agreement with our experimental results and previous reports.[24] The band gap decrease from the out-of-plane strain component is more prominent in the HS than in the monolayers, further supporting the notion that the interlayer interaction plays an important role in the band gap closing (Table S2). The strong band gap opening effect implies that in-plane strain dominates the band structure modulation and is responsible for the indirect band gap transition at higher pressures. The non-monotonic band gap variation also is captured by our theoretical calculation of conduction and valence band edge as functions of pressure (Figure S12) as well as hybridized band structure of the MoS_2/WS_2 heterostructure (Figure S13).

Strain-Modulation of Charge and Energy Transfers. In order to decipher the pressure-evolution of the interlayer interaction in the heterostructure, the experimentally measured PL intensity ratios between the HS and the monolayers (I_{HS}/I_{1L}; η), were extracted for MoS_2 and WS_2, respectively, as a function of pressure (Figure 3b). At pressures below ≈4 GPa, the η value of the MoS_2 remains close to unity with a marginal decrease. On the other hand, η_{WS2} is significantly lower than unity at ≈0.7 GPa and drastically decreases with pressure. The

https://doi.org/10.1021/acsami.2c10982
ACS Appl. Mater. Interfaces 2022, 14, 46841−46849

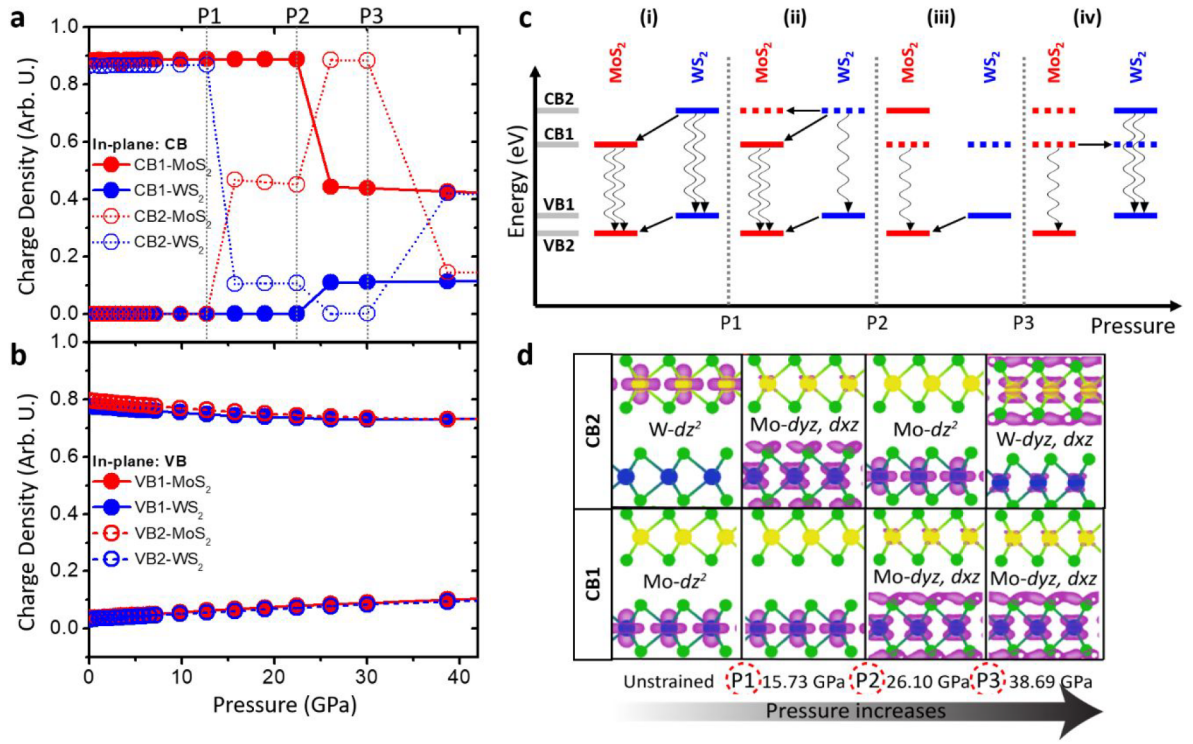

Figure 4. Pressure-dependent charge and energy transfers of the MoS_2/WS_2 heterobilayer. (a,b) Charge density at (a) conduction band and (b) valence band as a function of pressure along the in-plane direction. (c) Schematics demonstrating the charge density and charge transfers with increasing pressure. Straight and wavy arrows indicate the charge transfer and radiative decay, respectively. (d) Band-decomposed charge densities of the MoS_2/WS_2 heterostructure, superimposed with the side view of MoS_2 (bottom)/WS_2 (top) heterostructure. P1, P2, and P3 are representative pressure points where significant changes occur in the charge or orbital contribution to the conduction band, which correspond to ≈13 GPa, ≈22 GPa, and ≈30 GPa, respectively.

asymmetric PL quenching of the higher-bandgap layer (i.e., $\eta_{WS2} < 1$, whereas $\eta_{MoS2} \approx 1$) indicates that the ET is the dominating charge dynamics across the vdW interface.[52] In a type-II vdW heterobilayer such as MoS_2/WS_2, PL intensity quenching in the heterobilayer compared to that in each monolayer is indicative of separation of photoexcited carriers, i.e., CT.[14,53,54] On the other hand, an asymmetrically predominant PL quenching in a larger-band gap layer suggests ET, where both photoexcited electrons and holes transfer. Here, the ET is suggested to be the charge transfer dominant (Dexter) type other than the resonance dominant (Förster) type, as (i) the monolayers and excitation are not in resonance, and (ii) the heterobilayer's band extrema hybridize with increased pressure, as will be discussed in the later section. Other effects can be ruled out from potential mechanisms for the PL intensity ratio: (i) no charge or energy transfer occurs from/to the Si/Al_2O_3 substrate or Ne PTM, and therefore, the PL intensity change due to free carrier concentration change (i.e., doping) is limited;[4,55] (ii) large, homogeneous single-crystal monolayers guarantee little in-flake and flake-to-flake variability; (iii) identical excitation power for all measurements rule out any power-dependence; and (iv) pressure-induced band gap change of ≈20 meV will have only limited influence on the resonance-driven PL enhancement.[11] With other factors ruled out, the difference between the heterostructure and monolayers can be interpreted as the effect of interlayer interactions. Surprisingly, above 4 GPa, the PL emission landscape of WS_2 changes while the η_{MoS2} ratio continues to decrease: the η_{WS2} begins to increase, exceeds that of lower-pressure values, and eventually reaches unity at 7.7 GPa, suggesting that the interlayer ET has now subsided (Note S2 and Figure S14). The non-monotonic pressure-dependent evolution of the PL ratio η implies strong modulation of interlayer interactions under pressure, which lead to the modulation of the charge and energy transfers occurring at the heterostructure interface.

In order to investigate the origin of the non-monotonic modulation of ET, DFT band structure of the hybridized MoS_2/WS_2 heterostructure was calculated, and the orbital contributions in the CBM and VBM are analyzed (Figure S13). The intralayer A excitons (A_{MoS2} and A_{WS2}) of the monolayers are localized at the K-point in the momentum space of the heterostructure, as CBM (CB1) and the second valence band (VB2) come from MoS_2, and VBM (VB1) and the second conduction band (CB2) come from WS_2. The evolution of charge densities of the conduction and valence band valleys with the in-plane strain component is shown in Figure 4a and b, respectively. From ambient pressure to P1, the contribution of WS_2 electronic states in the CB2 and VB1 valley is less than that of the MoS_2 electronic states in the CB1 and VB2 valley, suggesting that both electron and hole densities are lower in WS_2. The asymmetric charge density shows an energy transfer from WS_2 to MoS_2, supporting our experimental findings (schematic view shown in Figure 4c). On further increasing the strain up to P2, the electron density of the CB2 valley (WS_2) decreases rapidly, implying an even larger energy transfer from WS_2 to MoS_2, which further explains the dramatic decrease of the WS_2 enhancement factor in experimental results.

https://doi.org/10.1021/acsami.2c10982
ACS Appl. Mater. Interfaces 2022, 14, 46841−46849

The charge contributions in CB1 and CB2 valleys of the heterostructure band are further analyzed in terms of the charge redistribution, as shown in Figure 4d. In the unstrained case, the CB1 (lower panel) and CB2 (upper panel) originate from the major contribution of d_{z^2} orbitals of Mo (blue) and W (yellow) atoms, respectively, showing strong localization of the band extrema contributions. With increasing pressure along the $x-y$ plane, the W−W and Mo−Mo atoms and their d_{z^2} orbitals come closer to each other (Figure S15) until the d_{z^2} orbitals overlap and hybridize at the P1 point for CB2 and the P2 point for CB1, respectively. The higher onset pressure for the charge transfer in the CB1 (MoS_2) valley is attributed to the less diffusive nature of Mo d_{z^2} orbitals. The charge transfer rate is also lower for CB1 compared to the CB2 valley, which is also experimentally reflected in the smaller change in the PL enhancement factor. After increasing the pressure from P2 up to P3, the rest of the charges in the CB2 valley transfer from WS_2 to the MoS_2 monolayer, which is responsible for the further decrease in the A_{WS2} and A_{MoS2} peak intensity in the heterostructure. However, above the P3 pressure, the η_{WS2} starts to increase again due to the increase in the population of WS_2 states at CB2 valley. On the other hand, the η_{MoS2} continues to decrease due to decreased MoS_2 states in CB1 valley.

The abrupt changes in the charge densities are investigated from the molecular orbital (MO) diagram at the K point for different strains, as shown in Note S3 and Figure S16.[56] At ≈22 GPa pressure (above P1), the orbital crossing happens in the vdW heterostructure between the CB2 and CB3 valleys, as shown in Figure 4d. Similarly, by applying ≈30 GPa pressure (above P2), the orbital switching occurs between CB1/CB2, CB3/CB4, and VB3/VB4 valleys. At ≈39 GPa pressure (above P3), CB2/CB3 orbital crossing takes place. These orbital switchings in individual layers are responsible for the drastic turnovers in the energy transfer and charge transfer in the MoS_2/WS_2 heterostructure. Most importantly, the out-of-plane strain is responsible for enhancing the interlayer orbital coupling, thereby greatly accelerating the strain-dependent changes in the orbital contributions and charge density.[23] We note that the pressures observed in the theoretical calculation are consistently higher than those in the experimental results. The discrepancy is due to the lack of pressure effect "acceleration" from the out-of-plane strain, since the calculations were carried out with the out-of-plane strain value fixed to zero for accessible computational loads.

CONCLUSION

In summary, compressive strain under hydrostatic pressure has been applied to the MoS_2/WS_2 heterobilayer to modulate their interlayer interactions and to control the interlayer charge and energy transfers. Enhanced interlayer interaction due to out-of-plane compressive strain was observed in blueshifts in Raman spectroscopy and photoluminescence spectroscopy, and Density Functional Theory was carried out to investigate the strain components' contributions. The out-of-plane strain component effectively blueshifts A′ Raman modes and decreases the optical band gap, indicative of the strong interlayer interaction. The PL enhancement factor for WS_2 decreases by the factor of 5 up to 4 GPa, but substantially increases by an order of magnitude up to 7.7 GPa. DFT calculations reveal that the non-monotonic evolution of the enhancement factor is a result of the orbital and switching and charge density change in the heterostructure's band extrema. Our findings highlight an effective way of controlling the interlayer energy and charge transfer in the 2D heterobilayer by compressive strain, thereby opening opportunities to mechanically modulate excitonic device functionalities.

METHODS

Preparation of the Heterobilayer Sample. Bulk MoS_2 and WS_2 crystals (2D Semiconductors) were mechanically exfoliated onto Si/SiO_2 substrates, and then evaporated with 50-nm-thick gold at a rate of 1 Å s^{-1} using an e-beam evaporator. A thermal release tape was then attached and peeled to isolate the topmost monolayers and the Au film.[38] The monolayer-Au films were then thermally released on desired target substrates (SiO_2/Si), where chemically etching the gold film using a potassium iodide/iodine (KI/I_2) solution resulted in single-crystal monolayers with 100−400 μm lateral size. Finally, the monolayers were rinsed with acetone and isopropyl alcohol (IPA) to remove any remaining residues, and thermally annealed at high vacuum. For stacking and transferring the heterobilayer, a PDMS stamp with a PPC adhesion layer was used to first pick up the WS_2 monolayer from the silicon substrate. The WS_2 monolayer was aligned and contacted with the MoS_2 monolayer and subsequently used to pick up the MoS_2 monolayer with a precision alignment. The picked-up heterobilayer was dropped onto the target substrate (Al_2O_3/Si placed on a diamond culet) by thermally melting the PPC. The PPC was eventually dissolved using acetone/isopropanol mixture.

Sample Preparation for Diamond Anvil Cell Experiments. A pair of 400 μm culet diamond anvils with ultralow fluorescence background were used in a symmetric DAC for the experiments. A Re gasket was preindented to ≈45 μm thickness, and subsequently a ≈230-μm-diameter hole was drilled at the very center of the indentation to form a sample chamber. A 10-μm-thick polished single-crystal Si chip (University Wafers) was deposited with 25-nm-thick Al_2O_3 using atomic layer deposition (ALD), cleaved into a desirable size, and placed onto one of the culets. After transferring the heterobilayer sample on the Si/Al_2O_3 substrate, ultrahigh-purity Ne pressure medium (99.999%, Airgas) was loaded into the sample chamber using a home-built gas loading system in the Mineral Physics Laboratory at The University of Texas at Austin. The pressure before and after each spectroscopic measurement was monitored by measuring the R_1 fluorescence line of the ruby sphere placed near the sample.[57] The pressure uncertainty is expected to be below 1% throughout the pressure range.[57,58]

Optical Characterization. Raman and PL spectroscopic measurements were carried out using the Renishaw inVia micro-Raman system at the Mineral Physical Laboratory at the University of Texas at Austin. A focused laser beam with a wavelength of 532 nm, spot size of ≈1 μm and incident power <5 mW at the sample position was used for the measurements. The spectral resolution in Raman measurements is ≈1.3 cm^{-1}. Lorentzian and Gaussian fittings were carried out to extract peak parameters from Raman and PL spectra, respectively.

Theoretical Calculations. Theoretical calculations of the monolayers and heterostructure of TMDCs were performed using first-principle density functional theory (DFT) as implemented in the Vienna Ab Initio Simulation Package (VASP).[59,60] All-electron projector augmented wave (PAW) potentials[61,62] were used to describe electron−ion interactions. The electronic exchange and correlation potential terms were represented by the Perdew−Burke−Ernzerhof (PBE)[63] generalized gradient approximation (GGA). The Kohn−Sham orbitals were expanded in the plane wave basis sets with an energy cutoff of 500 eV. All monolayers and heterostructure were relaxed using the conjugate-gradient method until the Hellmann−Feynman forces on every atom were less than 0.005 eV $Å^{-1}$. A well converged Monkhorst−Pack (MP)[64] k-grid of 12 × 12 × 1 was used to sample the Brillouin zone (BZ). To avoid spurious interactions between the periodically repeated images, a vacuum of 20 Å was used along the z-axis. The weak van der Waal (vdW) interaction between the layers was incorporated by the Grimme's PBE-D2 exchange functional.[65] The Raman modes of monolayers and heterostructure of

https://doi.org/10.1021/acsami.2c10982
ACS Appl. Mater. Interfaces 2022, 14, 46841−46849

TMDCs were calculated by using the density functional perturbation theory (DFPT).[66] To obtain accurate quasiparticle band structure and the correct description of the optical properties of the monolayers and heterostructure of TMDCs, many-body interactions should be taken into account in the calculations. The single shot GW (i.e., G0W0) calculation,[67] based on the many-body perturbation theory, was performed to get the quasiparticle information. Finally, we carried out the Bethe−Salpeter equation (BSE) calculations on top of G0W0 in order to get the information on excitonic effects in the optical absorption using the Tamm-Dancoff approximation.[68]

The frequency dependent macroscopic dielectric function by BSE is given by the equation[69]

$$\mathrm{Im}[\varepsilon_{\mathrm{BSE}}(\omega)] = \frac{16\pi e^2}{\omega^2}\sum_{S} |\langle 0|\vec{A}\cdot\vec{u}|\varphi_{cv}^{S}\rangle|^2 \delta(E_S - \omega) \quad (1)$$

where φ_{cv}^{S} and E_S are the excitonic wave function and energy, respectively for the excitonic state S. $\vec{A}$ is the polarization vector and $\vec{u}$ is the velocity operator between conduction and valence energy state. The BSE only give the information on direct transition.

For GW calculations, a k-mesh of 12 × 12 × 1 within the MP scheme was used for monolayers and the heterostructure system. The energy cutoff for the wave functions and response functions were set to be 500 and 200 eV, respectively, in BSE calculations. A well converged 432 empty bands and 50 frequency grid points were taken in the calculations. The 9 highest occupied valence bands and 18 lowest unoccupied conduction bands were included for excitonic states.

■ ASSOCIATED CONTENT

Data Availability Statement

The data supporting the findings of this work are available within the paper and Supporting Information, as well as from the corresponding authors upon reasonable request.

Supporting Information

The Supporting Information is available free of charge at https://pubs.acs.org/doi/10.1021/acsami.2c10982.

Pressure-dependent Raman and PL spectra; Details of theoretical calculation of strain and corresponding evolution of Raman spectra and band gap; Detailed schematic for charge densities and molecular orbital diagrams (PDF)

■ AUTHOR INFORMATION

Corresponding Authors

Joon-Seok Kim − *Department of Materials Science and Engineering, Northwestern University, Evanston, Illinois 60208, United States; Microelectronics Research Center, The University of Texas at Austin, Austin, Texas 78758, United States;* orcid.org/0000-0003-2395-7588; Email: joonseok.kim@northwestern.edu

Abhishek Singh − *Materials Research Centre, Indian Institute of Science, Bangalore 560012, India*; Email: abhishek@mrc.iisc.ernet.in

Deji Akinwande − *Microelectronics Research Center, The University of Texas at Austin, Austin, Texas 78758, United States;* orcid.org/0000-0001-7133-5586; Email: deji@ece.utexas.edu

Jung-Fu Lin − *Department of Geological Sciences, Jackson School of Geosciences, The University of Texas at Austin, Austin, Texas 78712, United States*; Email: afu@jsg.utexas.edu

Authors

Nikhilesh Maity − *Materials Research Centre, Indian Institute of Science, Bangalore 560012, India*

Myungsoo Kim − *Microelectronics Research Center, The University of Texas at Austin, Austin, Texas 78758, United States*

Suyu Fu − *Department of Geological Sciences, Jackson School of Geosciences, The University of Texas at Austin, Austin, Texas 78712, United States*

Rinkle Juneja − *Materials Research Centre, Indian Institute of Science, Bangalore 560012, India*

Complete contact information is available at: https://pubs.acs.org/10.1021/acsami.2c10982

Author Contributions

J.-S.K., D.A., and J.-F.L. conceived the original idea for the study. J.-S.K. designed the experiments, performed pressure-dependent Raman and PL measurements, and analyzed the data. M.K. provided large-scale exfoliated 2D materials, and S.F. helped to load neon pressure medium to the diamond anvil cell. All experimental work was conducted at the University of Texas at Austin. N.M. and A.S. designed the theoretical calculations and corresponding analysis. N.M. and R.J. conducted theoretical calculations. A.S., D.A., and J.-F.L. coordinated and supervised the research. All authors contributed to the article based on the draft written by J.-S.K.

Notes

The authors declare no competing financial interest.

■ ACKNOWLEDGMENTS

J.-S.K. and D.A. acknowledge support from the Defense Threat Reduction Agency (DTRA). J.-S.K. acknowledge support from NSF MRSEC program (DMR-1720139), and M.K. from NSF NASCENT ERC Center, respectively. N.M., R.J., and A.S. thank Materials Research Centre and Thematic Unit of Excellence, Indian Institute of Science, for providing the computational facilities. N.M., R.J., and A.S. acknowledge the support from Institute of Eminence (IoE) MHRD grant of Indian Institute of Science, and the grant from DST Korea. J.F.L. acknowledges support for the Renishaw inVia Raman system from Department of Geological Sciences and Jackson School of Geosciences at the University of Texas at Austin.

■ REFERENCES

(1) High, A. A.; Novitskaya, E. E.; Butov, L. V.; Hanson, M.; Gossard, A. C. Control of Exciton Fluxes in an Excitonic Integrated Circuit. *Science (1979)* **2008**, *321* (5886), 229−231.

(2) Butov, L. V. Excitonic Devices. *Superlattices Microstruct.* **2017**, *108*, 2−26.

(3) Britnell, L.; Ribeiro, R. M.; Eckmann, A.; Jalil, R.; Belle, B. D.; Mishchenko, A.; Kim, Y. J.; Gorbachev, R. V.; Georgiou, T.; Morozov, S. V.; Grigorenko, A. N.; Geim, A. K.; Casiraghi, C.; Castro Neto, A. H.; Novoselov, K. S. Strong Light-Matter Interactions in Heterostructures of Atomically Thin Films. *Science (1979)* **2013**, *340* (6138), 1311−1314.

(4) Mak, K. F.; He, K.; Lee, C.; Lee, G. H.; Hone, J.; Heinz, T. F.; Shan, J. Tightly Bound Trions in Monolayer MoS2. *Nat. Mater.* **2013**, *12* (3), 207−211.

(5) Geim, A. K.; Grigorieva, I. V. Van Der Waals Heterostructures. *Nature* **2013**, *499* (7459), 419−425.

(6) Unuchek, D.; Ciarrocchi, A.; Avsar, A.; Watanabe, K.; Taniguchi, T.; Kis, A. Room-Temperature Electrical Control of Exciton Flux in a van Der Waals Heterostructure. *Nature* **2018**, *560* (7718), 340−344.

(7) Jauregui, L. A.; Joe, A. Y.; Pistunova, K.; Wild, D. S.; High, A. A.; Zhou, Y.; Scuri, G.; de Greve, K.; Sushko, A.; Yu, C. H.; Taniguchi, T.; Watanabe, K.; Needleman, D. J.; Lukin, M. D.; Park, H.; Kim, P. Electrical Control of Interlayer Exciton Dynamics in Atomically Thin Heterostructures. *Science (1979)* **2019**, *366* (6467), 870−875.
(8) Unuchek, D.; Ciarrocchi, A.; Avsar, A.; Sun, Z.; Watanabe, K.; Taniguchi, T.; Kis, A. Valley-Polarized Exciton Currents in a van Der Waals Heterostructure. *Nat. Nanotechnol.* **2019**, *14* (12), 1104−1109.
(9) Hong, X.; Kim, J.; Shi, S.-F.; Zhang, Y.; Jin, C.; Sun, Y.; Tongay, S.; Wu, J.; Zhang, Y.; Wang, F. Ultrafast Charge Transfer in Atomically Thin MoS2/WS2 Heterostructures. *Nat. Nanotechnol.* **2014**, *9* (9), 682−686.
(10) Zhu, H.; Wang, J.; Gong, Z.; Kim, Y. D.; Hone, J.; Zhu, X. Y. Interfacial Charge Transfer Circumventing Momentum Mismatch at Two-Dimensional van Der Waals Heterojunctions. *Nano Lett.* **2017**, *17* (6), 3591−3598.
(11) Kozawa, D.; Carvalho, A.; Verzhbitskiy, I.; Giustiniano, F.; Miyauchi, Y.; Mouri, S.; Castro Neto, A. H.; Matsuda, K.; Eda, G. Evidence for Fast Interlayer Energy Transfer in MoSe 2 /WS 2 Heterostructures. *Nano Lett.* **2016**, *16* (7), 4087−4093.
(12) Xu, W.; Kozawa, D.; Liu, Y.; Sheng, Y.; Wei, K.; Koman, V. B.; Wang, S.; Wang, X.; Jiang, T.; Strano, M. S.; Warner, J. H. Determining the Optimized Interlayer Separation Distance in Vertical Stacked 2D WS 2 :HBN:MoS 2 Heterostructures for Exciton Energy Transfer. *Small* **2018**, *14* (13), 1703727.
(13) Wu, L.; Chen, Y.; Zhou, H.; Zhu, H. Ultrafast Energy Transfer of Both Bright and Dark Excitons in 2D van Der Waals Heterostructures beyond Dipolar Coupling. *ACS Nano* **2019**, *13* (2), 2341−2348.
(14) Jin, C.; Ma, E. Y.; Karni, O.; Regan, E. C.; Wang, F.; Heinz, T. F. Ultrafast Dynamics in van Der Waals Heterostructures. *Nature Nanotechnology* **2018**, *13*, 994−1003.
(15) Tongay, S.; Fan, W.; Kang, J.; Park, J.; Koldemir, U.; Suh, J.; Narang, D. S.; Liu, K.; Ji, J.; Li, J.; Sinclair, R.; Wu, J. Tuning Interlayer Coupling in Large-Area Heterostructures with CVD-Grown MoS 2 and WS 2 Monolayers. *Nano Lett.* **2014**, *14* (6), 3185−3190.
(16) Bakharev, P. V.; Huang, M.; Saxena, M.; Lee, S. W.; Joo, S. H.; Park, S. O.; Dong, J.; Camacho-Mojica, D. C.; Jin, S.; Kwon, Y.; Biswal, M.; Ding, F.; Kwak, S. K.; Lee, Z.; Ruoff, R. S. Chemically Induced Transformation of Chemical Vapour Deposition Grown Bilayer Graphene into Fluorinated Single-Layer Diamond. *Nat. Nanotechnol.* **2020**, *15* (1), 59−66.
(17) Liu, X. C.; Zhao, S.; Sun, X.; Deng, L.; Zou, X.; Hu, Y.; Wang, Y. X.; Chu, C. W.; Li, J.; Wu, J.; Ke, F. S.; Ajayan, P. M. Spontaneous Self-Intercalation of Copper Atoms into Transition Metal Dichalcogenides. *Science Advances* **2020**, *6* (7), 1.
(18) Huttmann, F.; Martínez-Galera, A. J.; Caciuc, V.; Atodiresei, N.; Schumacher, S.; Standop, S.; Hamada, I.; Wehling, T. O.; Blügel, S.; Michely, T. Tuning the van Der Waals Interaction of Graphene with Molecules via Doping. *Phys. Rev. Lett.* **2015**, *115* (23), 236101.
(19) Meng, Y.; Wang, T.; Jin, C.; Li, Z.; Miao, S.; Lian, Z.; Taniguchi, T.; Watanabe, K.; Song, F.; Shi, S. F. Electrical Switching between Exciton Dissociation to Exciton Funneling in MoSe2/WS2 Heterostructure. *Nat. Commun.* **2020**, *11* (1), 1−6.
(20) Rosenberger, M. R.; Chuang, H.-J.; McCreary, K. M.; Hanbicki, A. T.; Sivaram, S. v.; Jonker, B. T. Nano-"Squeegee" for the Creation of Clean 2D Material Interfaces. *ACS Appl. Mater. Interfaces* **2018**, *10* (12), 10379−10387.
(21) Bhattacharyya, S.; Singh, A. K. Semiconductor-Metal Transition in Semiconducting Bilayer Sheets of Transition-Metal Dichalcogenides. *Physical Review B - Condensed Matter and Materials Physics* **2012**, *86* (7), 1−7.
(22) Pak, S.; Lee, J.; Lee, Y. W.; Jang, A. R.; Ahn, S.; Ma, K. Y.; Cho, Y.; Hong, J.; Lee, S.; Jeong, H. Y.; Im, H.; Shin, H. S.; Morris, S. M.; Cha, S.; Sohn, J. I.; Kim, J. M. Strain-Mediated Interlayer Coupling Effects on the Excitonic Behaviors in an Epitaxially Grown MoS2/WS2van Der Waals Heterobilayer. *Nano Lett.* **2017**, *17* (9), 5634−5640.
(23) Nayak, A. P.; Bhattacharyya, S.; Zhu, J.; Liu, J.; Wu, X.; Pandey, T.; Jin, C.; Singh, A. K.; Akinwande, D.; Lin, J.-F. Pressure-Induced Semiconducting to Metallic Transition in Multilayered Molybdenum Disulphide. *Nat. Commun.* **2014**, *5* (1), 3731.
(24) Kim, J.-S.; Ahmad, R.; Pandey, T.; Rai, A.; Feng, S.; Yang, J.; Lin, Z.; Terrones, M.; Banerjee, S. K.; Singh, A. K.; Akinwande, D.; Lin, J.-F. Towards Band Structure and Band Offset Engineering of Monolayer Mo (1- x) W (x) S 2 via Strain. *2D Materials* **2018**, *5* (1), 015008.
(25) Nayak, A. P.; Pandey, T.; Voiry, D.; Liu, J.; Moran, S. T.; Sharma, A.; Tan, C.; Chen, C.; Li, L.-J.; Chhowalla, M.; Lin, J.-F.; Singh, A. K.; Akinwande, D. Pressure-Dependent Optical and Vibrational Properties of Monolayer Molybdenum Disulfide. *Nano Lett.* **2015**, *15* (1), 346−353.
(26) Nayak, A. P.; Yuan, Z.; Cao, B.; Liu, J.; Wu, J.; Moran, S. T.; Li, T.; Akinwande, D.; Jin, C.; Lin, J.-F. Pressure-Modulated Conductivity, Carrier Density, and Mobility of Multilayered Tungsten Disulfide. *ACS Nano* **2015**, *9* (9), 9117−9123.
(27) Yankowitz, M.; Jung, J.; Laksono, E.; Leconte, N.; Chittari, B. L.; Watanabe, K.; Taniguchi, T.; Adam, S.; Graf, D.; Dean, C. R. Dynamic Band-Structure Tuning of Graphene Moiré Superlattices with Pressure. *Nature* **2018**, *557* (7705), 404−408.
(28) Padhi, B.; Phillips, P. W. Pressure-Induced Metal-Insulator Transition in Twisted Bilayer Graphene. *Phys. Rev. B* **2019**, *99* (20), 205141.
(29) Meng, X.; Pandey, T.; Jeong, J.; Fu, S.; Yang, J.; Chen, K.; Singh, A.; He, F.; Xu, X.; Zhou, J.; Hsieh, W.-P.; Singh, A. K.; Lin, J.-F.; Wang, Y. Thermal Conductivity Enhancement in MoS2 under Extreme Strain. *Phys. Rev. Lett.* **2019**, *122* (15), 155901.
(30) Kim, J.-S.; Moran, S. T.; Nayak, A. P.; Pedahzur, S.; Ruiz, I.; Ponce, G.; Rodriguez, D.; Henny, J.; Liu, J.; Lin, J.-F.; Akinwande, D. High Pressure Raman Study of Layered Mo 0.5 W 0.5 S 2 Ternary Compound. *2D Materials* **2016**, *3* (2), 025003.
(31) Juneja, R.; Shinde, R.; Singh, A. K. Pressure-Induced Topological Phase Transitions in CdGeSb 2 and CdSnSb 2. *J. Phys. Chem. Lett.* **2018**, *9* (9), 2202−2207.
(32) Kim, J. S.; Juneja, R.; Salke, N. P.; Palosz, W.; Swaminathan, V.; Trivedi, S.; Singh, A. K.; Akinwande, D.; Lin, J. F. Structural, Vibrational, and Electronic Topological Transitions of Bi1.5Sb0.5-Te1.8Se1.2under Pressure. *J. Appl. Phys.* **2018**, *123* (11), 115903.
(33) Pandey, T.; Nayak, A. P.; Liu, J.; Moran, S. T.; Kim, J.-S.; Li, L.-J.; Lin, J.-F.; Akinwande, D.; Singh, A. K. Pressure-Induced Charge Transfer Doping of Monolayer Graphene/MoS 2 Heterostructure. *Small* **2016**, *12* (30), 4063−4069.
(34) Xia, J.; Yan, J.; Wang, Z.; He, Y.; Gong, Y.; Chen, W.; Sum, T. C.; Liu, Z.; Ajayan, P. M.; Shen, Z. Strong Coupling and Pressure Engineering in WSe2-MoSe2 Heterobilayers. *Nat. Phys.* **2020**, 1−7.
(35) Fu, X.; Li, F.; Lin, J.-F.; Gong, Y.; Huang, X.; Huang, Y.; Gao, H.; Zhou, Q.; Cui, T. Coupling-Assisted Renormalization of Excitons and Vibrations in Compressed MoSe 2 -WSe 2 Heterostructure. *J. Phys. Chem. C* **2018**, *122* (10), 5820−5828.
(36) Das, S. Two Dimensional Electrostrictive Field Effect Transistor (2D-EFET): A Sub-60mV/Decade Steep Slope Device with High ON Current. *Sci. Rep.* **2016**, *6* (1), 34811.
(37) Yu, F.; Liu, Q.; Gan, X.; Hu, M.; Zhang, T.; Li, C.; Kang, F.; Terrones, M.; Lv, R. Ultrasensitive Pressure Detection of Few-Layer MoS 2. *Adv. Mater.* **2017**, *29* (4), 1603266.
(38) Desai, S. B.; Madhvapathy, S. R.; Amani, M.; Kiriya, D.; Hettick, M.; Tosun, M.; Zhou, Y.; Dubey, M.; Ager, J. W.; Chrzan, D.; Javey, A. Gold-Mediated Exfoliation of Ultralarge Optoelectronically-Perfect Monolayers. *Adv. Mater.* **2016**, *28* (21), 4053−4058.
(39) Kim, K.; Yankowitz, M.; Fallahazad, B.; Kang, S.; Movva, H. C. P. P.; Huang, S.; Larentis, S.; Corbet, C. M.; Taniguchi, T.; Watanabe, K.; Banerjee, S. K.; LeRoy, B. J.; Tutuc, E. Van Der Waals Heterostructures with High Accuracy Rotational Alignment. *Nano Lett.* **2016**, *16* (3), 1989−1995.
(40) Wu, D.; Li, X.; Luan, L.; Wu, X.; Li, W.; Yogeesh, M. N.; Ghosh, R.; Chu, Z.; Akinwande, D.; Niu, Q.; Lai, K. Uncovering Edge

https://doi.org/10.1021/acsami.2c10982
ACS Appl. Mater. Interfaces 2022, 14, 46841−46849

States and Electrical Inhomogeneity in MoS 2 Field-Effect Transistors. *Proc. Natl. Acad. Sci. U. S. A.* **2016**, *113* (31), 8583−8588.
(41) Uddin, S. Z.; Kim, H.; Lorenzon, M.; Yeh, M.; Lien, D.-H.; Barnard, E. S.; Htoon, H.; Weber-Bargioni, A.; Javey, A. Neutral Exciton Diffusion in Monolayer MoS 2. *ACS Nano* **2020**, *14*, 13433.
(42) Klotz, S.; Chervin, J.-C.; Munsch, P.; le Marchand, G. Hydrostatic Limits of 11 Pressure Transmitting Media. *J. Phys. D: Appl. Phys.* **2009**, *42* (7), 075413.
(43) Anzellini, S.; Wharmby, M. T.; Miozzi, F.; Kleppe, A.; Daisenberger, D.; Wilhelm, H. Quasi-Hydrostatic Equation of State of Silicon up to 1 Megabar at Ambient Temperature. *Sci. Rep.* **2019**, *9* (1), 15537.
(44) Lin, J.-F.; Degtyareva, O.; Prewitt, C. T.; Dera, P.; Sata, N.; Gregoryanz, E.; Mao, H.-K.; Hemley, R. J. Crystal Structure of a High-Pressure/High-Temperature Phase of Alumina by in Situ X-Ray Diffraction. *Nat. Mater.* **2004**, *3* (6), 389−393.
(45) Welber, B.; Kim, C. K.; Cardona, M.; Rodriguez, S. Dependence of the Indirect Energy Gap of Silicon on Hydrostatic Pressure. *Solid State Commun.* **1975**, *17* (8), 1021−1024.
(46) Tongay, S.; Suh, J.; Ataca, C.; Fan, W.; Luce, A.; Kang, J. S.; Liu, J.; Ko, C.; Raghunathanan, R.; Zhou, J.; Ogletree, F.; Li, J.; Grossman, J. C.; Wu, J. Defects Activated Photoluminescence in Two-Dimensional Semiconductors: Interplay between Bound, Charged, and Free Excitons. *Sci. Rep.* **2013**, *3* (1), 1−5.
(47) Klein, J.; Kuc, A.; Nolinder, A.; Altzschner, M.; Wierzbowski, J.; Sigger, F.; Kreupl, F.; Finley, J. J.; Wurstbauer, U.; Holleitner, A. W.; Kaniber, M. Robust Valley Polarization of Helium Ion Modified Atomically Thin MoS2. *2D Materials* **2018**, *5* (1), 011007.
(48) Kim, H. J.; Yun, Y. J.; Yi, S. N.; Chang, S. K.; Ha, D. H. Changes in the Photoluminescence of Monolayer and Bilayer Molybdenum Disulfide during Laser Irradiation. *ACS Omega* **2020**, *5* (14), 7903−7909.
(49) Nayak, P. K.; Horbatenko, Y.; Ahn, S.; Kim, G.; Lee, J.-U.; Ma, K. Y.; Jang, A.-R.; Lim, H.; Kim, D.; Ryu, S.; Cheong, H.; Park, N.; Shin, H. S. Probing Evolution of Twist-Angle-Dependent Interlayer Excitons in MoSe 2 /WSe 2 van Der Waals Heterostructures. *ACS Nano* **2017**, *11* (4), 4041−4050.
(50) Lynch, R. W.; Drickamer, H. G. Effect of High Pressure on the Lattice Parameters of Diamond, Graphite, and Hexagonal Boron Nitride. *J. Chem. Phys.* **1966**, *44* (1), 181−184.
(51) Ye, Y.; Dou, X.; Ding, K.; Jiang, D.; Yang, F.; Sun, B. Pressure-Induced K-Λ Crossing in Monolayer WSe 2. *Nanoscale* **2016**, *8* (20), 10843−10848.
(52) Hill, H. M.; Rigosi, A. F.; Rim, K. T.; Flynn, G. W.; Heinz, T. F. Band Alignment in MoS 2 /WS 2 Transition Metal Dichalcogenide Heterostructures Probed by Scanning Tunneling Microscopy and Spectroscopy. *Nano Lett.* **2016**, *16* (8), 4831−4837.
(53) Lee, C. H.; Lee, G. H.; Van Der Zande, A. M.; Chen, W.; Li, Y.; Han, M.; Cui, X.; Arefe, G.; Nuckolls, C.; Heinz, T. F.; Guo, J.; Hone, J.; Kim, P. Atomically Thin p-n Junctions with van Der Waals Heterointerfaces. *Nature Nanotechnology* **2014**, *9* (9), 676−681.
(54) Chen, H.; Wen, X.; Zhang, J.; Wu, T.; Gong, Y.; Zhang, X.; Yuan, J.; Yi, C.; Lou, J.; Ajayan, P. M.; Zhuang, W.; Zhang, G.; Zheng, J. Ultrafast Formation of Interlayer Hot Excitons in Atomically Thin MoS2/WS2 Heterostructures. *Nature Communications* **2016**, *7* (1), 1−8.
(55) Zheng, B.; Zheng, W.; Jiang, Y.; Chen, S.; Li, D.; Ma, C.; Wang, X.; Huang, W.; Zhang, X.; Liu, H.; Jiang, F.; Li, L.; Zhuang, X.; Wang, X.; Pan, A. WO 3 -WS 2 Vertical Bilayer Heterostructures with High Photoluminescence Quantum Yield. *J. Am. Chem. Soc.* **2019**, *141*, 11754−11758.
(56) Singh, A.; Manjanath, A.; Singh, A. K. Engineering Defect Transition-Levels through the van Der Waals Heterostructure. *J. Phys. Chem. C* **2018**, *122* (42), 24475−24480.
(57) Chervin, J. C.; Canny, B.; Mancinelli, M. Ruby-Spheres as Pressure Gauge for Optically Transparent High Pressure Cells. *High Pressure Research* **2001**, *21* (6), 305−314.
(58) Mao, H. K.; Mao, W. L. Theory and Practice: Diamond-Anvil Cells and Probes for High-P-T Mineral Physics Studies. *Treatise on Geophysics: Second Edition* **2015**, *2*, 263−291.
(59) Kresse, G.; Furthmüller, J. Efficient Iterative Schemes for Ab Initio Total-Energy Calculations Using a Plane-Wave Basis Set. *Phys. Rev. B* **1996**, *54* (16), 11169−11186.
(60) Kresse, G.; Furthmüller, J. Efficiency of Ab-Initio Total Energy Calculations for Metals and Semiconductors Using a Plane-Wave Basis Set. *Comput. Mater. Sci.* **1996**, *6* (1), 15−50.
(61) Blöchl, P. E. Projector Augmented-Wave Method. *Phys. Rev. B* **1994**, *50* (24), 17953−17979.
(62) Kresse, G.; Joubert, D. From Ultrasoft Pseudopotentials to the Projector Augmented-Wave Method. *Phys. Rev. B* **1999**, *59* (3), 1758−1775.
(63) Perdew, J. P.; Burke, K.; Ernzerhof, M. Generalized Gradient Approximation Made Simple. *Phys. Rev. Lett.* **1996**, *77* (18), 3865−3868.
(64) Monkhorst, H. J.; Pack, J. D. Special Points for Brillouin-Zone Integrations. *Phys. Rev. B* **1976**, *13* (12), 5188−5192.
(65) Grimme, S. Semiempirical GGA-Type Density Functional Constructed with a Long-Range Dispersion Correction. *J. Comput. Chem.* **2006**, *27* (15), 1787−1799.
(66) Gonze, X.; Vigneron, J.-P. Density-Functional Approach to Nonlinear-Response Coefficients of Solids. *Phys. Rev. B* **1989**, *39* (18), 13120−13128.
(67) Shishkin, M.; Kresse, G. Implementation and Performance of the Frequency-Dependent GW Method within the PAW Framework. *Phys. Rev. B* **2006**, *74* (3), 035101.
(68) Rohlfing, M.; Louie, S. G. Electron-Hole Excitations in Semiconductors and Insulators. *Phys. Rev. Lett.* **1998**, *81* (11), 2312−2315.
(69) Maity, N.; Srivastava, P.; Mishra, H.; Shinde, R.; Singh, A. K. Anisotropic Interlayer Exciton in GeSe/SnS van Der Waals Heterostructure. *J. Phys. Chem. Lett.* **2021**, *12* (7), 1765−1771.

https://doi.org/10.1021/acsami.2c10982
ACS Appl. Mater. Interfaces 2022, 14, 46841−46849